scientific reports

Check for updates

OPEN

In-orbit monitoring for dynamic detector-oriented containment of TID-induced degradation in CMOS-TDI sensor systems

Johannes Buschek[1]✉, Evgeny Chernyavskiy[1], Gerhard Kahmen[2] & Andreas Eckardt[1]

Space-borne CMOS-based sensor systems with time delay and integration (TDI) functionality are susceptible to the radiation environment in orbit. Total ionizing dose (TID) impacts CMOS detector structures and considerably deteriorates performance and image quality. We investigated dynamic detector-oriented methods to counteract TID-induced degradation effects. We equipped the CMOS-TDI detector system with in-orbit monitoring capabilities applying charge injection and subsampling to reveal inherent detector operation feedback and enable system adaptation during operation. Thus, the impact of radiation was significantly contained. The charge transfer efficiency (CTE) accordingly reached the pre-radiation level. The relative charge loss was reduced by a factor of 8.1, yielding a substantial improvement in CTE, and hence, in the geometric resolution. We further applied device compact modeling, aiming for a comprehensive system model to facilitate adequate prediction of performance degradation caused by TID, which could be generally applied to upcoming designs of the CMOS-TDI detector family after external validation.

Keywords Charge injection, CMOS-TDI, Degradation, In-orbit monitoring, Equivalent time sampling, Radiation, Subsampling, Total ionizing dose

State-of-the-art space-borne CMOS-based sensor systems are designed for earth observation or planetary exploration and are exposed to the radiation environment in orbit[1]. Protons, electrons, low-energy heavy ions, and galactic cosmic rays cause both single event effects (SEEs) and cumulative radiation effects[2,3]. SEEs are random particle-induced events that range from transient upsets to persistent conditions, such as latch-up, with performance and/or functional impact. Common strategies to mitigate destructive SEEs are hardened device structures and circuit-level redundancies[4]. Cumulative radiation effects lead to changes in the semiconductor, which result in gradual, systematic performance deterioration. One distinguishes between displacement damage (DD), describing lattice defects related to non-ionizing radiation, and total ionizing dose (TID), referring to the cumulative charge build up resulting from exposure to ionizing radiation[5,6].

Using in-orbit calibration systems is a common practice for managing the gradual degradation in image quality. Various techniques are implemented to update operating parameters to restore system accuracy during operation. The visible and infrared system on the NOAA-20 satellite (VIIRS), for example, utilizes an onboard solar diffuser combined with lunar data to correct long-term gain trends, whereas the Chinese set of remote sensing satellites, SuperView-1, operates with multiple ground permanent artificial targets to verify the radiometric performance at the system level[7,8].

The CMOS-TDI detector system is designed for future satellite missions, that aim for high-resolution reconnaissance with a ground sampling distance (GSD) well below 50 cm. It employs a high-voltage CMOS process for the embedded charge coupled device (eCCD), enabling the transport of a large amount of charge and thereby resolving complex image scenes with a high dynamic range (Fig. 1f). The readout integrated circuit (ROIC) is fabricated in a high-speed BiCMOS process, ensuring fast readout of the image data. The combination of the technologies creates flexible and highly integrated detector modules, utilizing TDI operation to fulfill the growing demands on signal-to-noise ratio (SNR), spatial resolution, and on-chip processing (Fig. 1a)[9–11]. The improvements in system accuracy are accompanied by higher sensitivity and susceptibility to radiation, underscoring the need for further research into methods to mitigate performance degradation in orbit. The

[1]Department High-Speed Electronics, Institute of Space Research, German Aerospace Center (DLR), Rutherfordstraße 2, 12489 Berlin, Germany. [2]Leibniz Institute for High Performance Microelectronics (IHP), Im Technologiepark 25, 15236 Frankfurt (Oder), Germany. ✉email: johannes.buschek@dlr.de

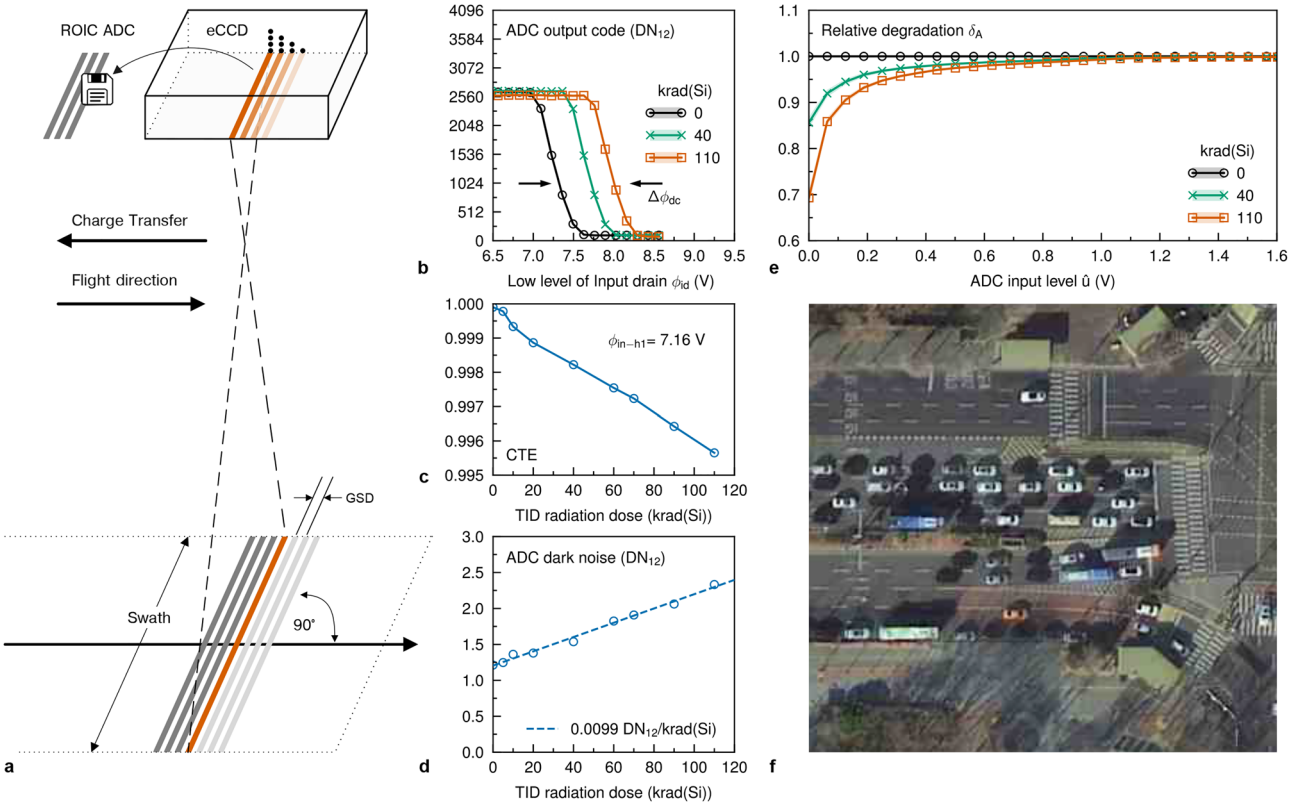


Fig. 1. The CMOS-TDI imaging system in orbit and experimental measurement of the impact of TID. (**a**) The concept of a TDI line scanner, which effectively extends the exposure time by a charge transfer opposite to the flight direction. (**b**) Charge injection threshold for different radiation doses, illustrating the flatband voltage shift in the eCCD, which leads to a misalignment of the eCCD charge domain. (**c**) CTE by increasing radiation dose degrades the geometric resolution of the detector system; a CTE of 1 represents the theoretical maximum. (**d**) ROIC ADC dark noise vs. radiation dose, increasing by a factor of 1.93 at a radiation dose of 110 krad(Si) and, in turn, reducing the dynamic range. (**e**) ROIC ADC transfer function degradation for different radiation doses, showing a further reduction in the dynamic range and a change in sensitivity, which result in non-linear effects in the acquired image data. (**f**) Jamsil-dong, Songpa-gu, Seoul, South Korea, road crossing next to the Jamsil Olympic Stadium, photographed in 2026 by the Korea Multi-Purpose Satellite-7 (KompSat-7) with a GSD of 30 cm and a radiometric resolution of 12 bit. Source: Korea AeroSpace Administration (KASA)[20].

common approaches are limited to changes in the focal plane electronics (FPE), they consist of evaluating system level deviations to estimate and correct performance parameters through gain changes or solely even via image post-processing[12]. They do not target the detector operation and therefore cannot counteract the radiation-induced performance degradation of the sensor. The degradation of the image quality of the CMOS-TDI detector system in the radiation environment in orbit mainly relates to TID-induced changes in CCD structures and deterioration of the performance of CMOS analog-to-digital converter (ADC) circuits[13–17]. TID significantly impacts essential system parameters, such as the dynamic range, SNR, sensitivity, and modulation transfer function (MTF), and may result in a complete detector malfunction due to charge buildup. DD effects mainly result in silicon bulk damage, increased dark current and degraded charge transfer efficiency (CTE) related to CCD-on-CMOS sensors, however, for the CMOS-TDI detector system it plays a marginal role in the performance compared to the TID-induced degradation due to the application and its inherent structure[18,19].

In the following, we investigate detector-oriented methods for the CMOS-TDI detector system to dynamically counteract radiation-induced degradation caused by TID. Design analysis, simulations, and detector measurements are conducted to identify system adaptation and monitoring options to achieve a constant image quality over the mission lifetime. We adapt system operation parameters to assess the extent to which the effects of TID can be overcome and develop a theoretical model to predict TID-induced degradation in the CMOS-TDI detector system.

Results and discussion

Impact of TID on the CMOS-TDI detector system

TID has an extensive impact on the CMOS-TDI detector system and on the resulting image quality. To assess the degradation of the eCCD and the ROIC circuitry, we performed experimental detector measurements using a set of iterative electrical tests during ^{60}Co (γ) irradiation on four different detectors to emulate the response of the sensor exposed to TID in orbit. We further conducted SPICE simulation of the eCCD and ROIC circuitry

to compare and validate the established device compact models. For further methodological details, see the Methods section at the end of this manuscript.

Linearity of the analog-to-digital converter (ADC)

The relative transfer function degradation was defined as the mean degradation, δ_A, of all four detectors for each radiation dose D, normalized to the pre-radiation result (Fig. 1e). The ADC transfer function was measured by using a converter-synchronized external input signal to emulate an eCCD output.

It revealed changes in the pattern of integrated nonlinearity (INL), the converter slope, and the zero-scale level. The observed transfer function degradation decreased sensitivity and, in combination with an increased noise, resulted in a notable reduction in dynamic range (Fig. 1d). The relative degradation δ_A appeared throughout the entire dynamic range, whereas the intensity of the TID-induced INL pattern varied slightly across the tested integrated circuits. The allocation of the observed degradation mechanism could be narrowed down to the comparator circuitry by simulation.

A change in sensitivity is common for TID-induced effects on CMOS ADCs, but the concrete error pattern highly depends on the complexity and the system architecture of the designed integrated circuit[16,17,21,22]. Further layout data analysis and parasitic extraction would be needed to investigate the specific circuit part causing the degradation. The observed increase in ROIC noise is in the range of common findings, where the magnitude of the increase varies between reported detector architectures[17].

Flatband voltage shift determination

The fill threshold during charge injection is a crucial measure of the eCCD input structure and enables the assessment of the charge domain alignment. To determine the n+ drain voltage level, at which charge carriers start to reach the depletion regions below the eCCD input gate ϕ_{in}, a specific fill threshold test was conducted iteratively between the irradiation intervals.

It revealed a noticeable TID-induced flatband voltage shift. Fig. 1b illustrates the voltage shift of the fill threshold, which could be assigned to the flatband voltage shift of the input transfer gate potential $\Delta\phi_{dc}$. Different values for frontside-illuminated (FSI) and backside-illuminated (BSI) eCCDs could be determined, with a larger change for BSI at the maximum radiation dose of 110 krad(Si). The flatband voltage shift, which occurs at all eCCD gates, distracted the alignment of the eCCD charge domain.

The observed voltage shift $\Delta\phi_{dc}$ can be explained by the accumulated charge in the gate oxide induced by ionized radiation. The finding is consistent with reports of similar processes[13,14,23]. The significant difference between FSI and BSI in flatband voltage shifts stems from the different manufacturing processes for the device types. The additional BSI fabrication steps create donor-like border traps at the silicon-oxide interface, shifting the flatband voltage as if a positive charge were present[24]. Thus, the absolute value of $\Delta\phi_{dc}$ is higher for BSI devices.

Activation energy and dark current

Changes on activation energy were measured by assessing the leakage current in a reverse-biased diode formed by the p-substrate and the n-well (eCCD buried channel) versus temperature. The dark level measurements on the detector system were performed with an integration time of 6.66 µs.

For the activation energy measurement, a mean reduction of ΔE_a of − 0.195 eV for BSI, and − 0.391 eV for FSI between non-irradiated and irradiated eCCDs (110 krad(Si)) was shown. We observed a marginal increase of 0.28 % of the eCCD dark level relative to the ADC full-scale at 110 krad(Si).

The thermal activation energies are characterized mainly by bulk dark current conditioned by trap-assistant carrier thermal generation. It indicates that the contribution from TID-generated surface states is marginal and that displacement damage (DD) has no significant effect within the investigated dose range. The difference in ΔE_a between BSI and FSI is related to more bulk volume for the tested FSI diode (p-substrate), and, in turn, more diffusion current in the non-depleted bulk compared to BSI[25]. To evaluate a dark current specification in electrons per pixel per second, additional tests with longer integration times are necessary.

Source follower characterization

The characterization of the source follower (SF) was conducted by assessing the DC transfer function between the drain of the conducting reset transistor and the resulting SF output voltage (Fig. 2d).

It showed a substantial degradation in the unused lower region ($U_d < 4.0$ V) and minor deviations inside the operation region (8.0 V < U_d < 11.0 V), which was expressed as SF gain loss ΔA_{sf} vs. radiation dose (Fig. 2b).

It aligns with common findings that the SF topology is relatively robust and tolerates radiation degradation with minimal impact on performance[26].

Overall view

The primary contributor to the performance degradation was CTE deterioration caused by misalignment of the eCCD charge domain. The observed ADC non-linearities were critical compared to the marginal SF gain loss.

Regarding the conducted tests, leakage current and subthreshold behavior are known transistor properties that are affected by TID[27,28]. At the system level, they increase overall power consumption and thus affect the thermal control loop of the focal plane array (FPA). However, we could not assess the effects on leakage current and subthreshold behavior, as any increase in leakage current is hardly distinguishable from dynamic switching losses due to the given lack of accuracy of the test setup. Although, Gamma rays emitted by ^{60}Co (γ) sources induce DD effects through the generation of secondary electrons, they can be disregarded in the structure of the examined detector system[29,30]. The CTE degradation is crucial, as CTE is directly linked to the MTF, a key metric of the magnitude response of an optical system at different spatial frequencies and, hence, image quality[31,32].

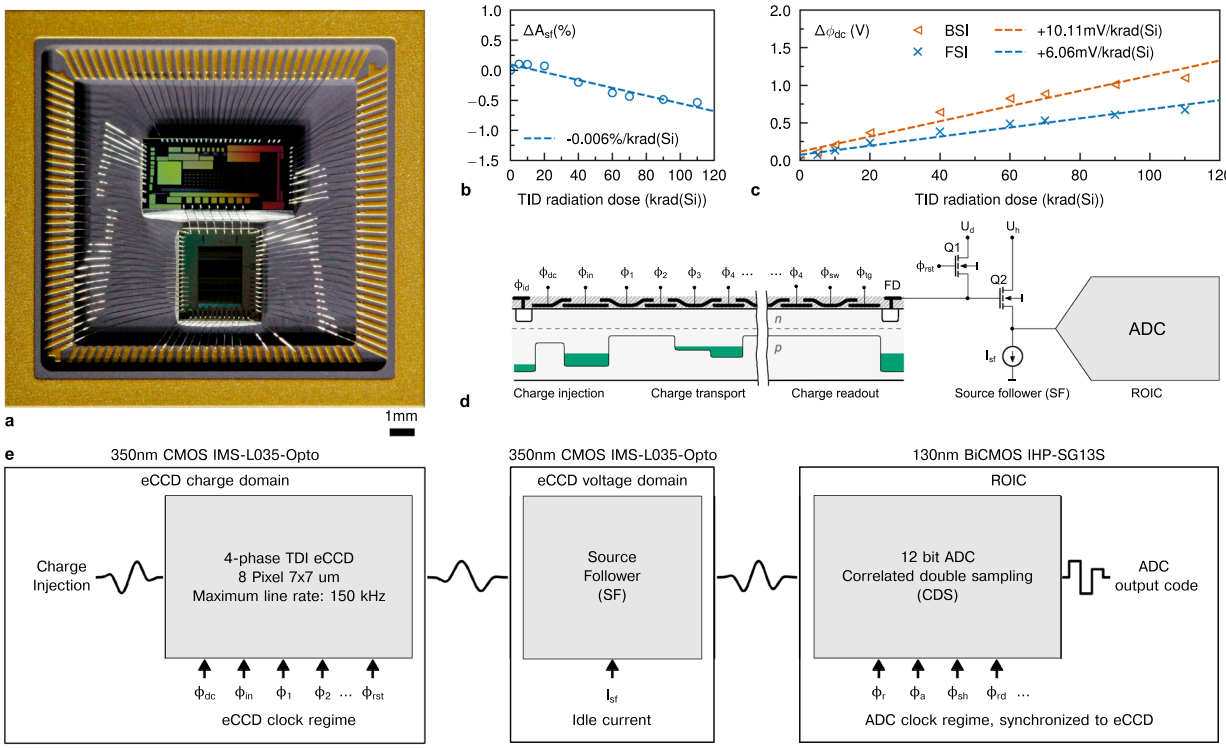


Fig. 2. The flexibility of the CMOS-TDI system. (**a**) CMOS-TDI detector system in a PGA-132 package with eCCD (top) and ROIC (bottom), picture of the analyzed sensor assembly, Credit: German Aerospace Center (DLR), WR-HGE. (**b**) SF gain loss by increasing radiation dose, showing a marginal change of -0.54 % at 110 krad(Si). (**c**) Flatband voltage shift for FSI and BSI detectors by increasing radiation dose, indicating 0.67 V for FSI, and 1.10 V for BSI at the maximum radiation dose of 110 krad(Si). (**d**) Physical structure of the eCCD from the injection side (left), with input transfer gate ϕ_{dc} and input summing well ϕ_{in} to the readout side (right), with output transfer gate ϕ_{tg}, output summing well ϕ_{sw}, and the floating diffusion (FD) including the subsequent source follower (SF) circuitry. (**e**) CMOS-TDI block diagram separated by domains and key parameters, the analog electrical input signal, created by charge injection, is converted into a digital ADC output code.

Post-processing methods can be applied to correct the ADC non-linearities. The TID-induced SF gain loss has a minimal and linear impact on the overall performance degradation of the CMOS-TDI detector system.

Adjustable parameters in the CMOS-TDI system to counteract degradation

The investigated version of the CMOS-TDI detector system consists of an 8-pixel test detector. It aims to achieve higher integration to improve signal integrity and incorporate complex functionality in a reduced form factor, resulting in an increased sensor operating speed up to 150 kHz and a reduction in overall FPA power consumption. System performance benefits from the separation into two distinct, specifically selected CMOS processes: 350 nm CMOS (IMS L035 Opto) for the eCCD and 130 nm BiCMOS (IHP SG13S) for the ROIC (Fig. 2a). The buried-channel eCCD is suitable for high-voltage operation, yielding a high full well capacity (FWC) of 150 ke-. The architecture of the 8-pixel test sensor employs a fill-and-spill structure for charge injection, and overlapping poly-gates ensure high CTE across selectable 128- or 256-stage TDI modes. After the eCCD readout circuitry (SF), the ROIC converts the eCCD signal into a corresponding 12 bit digital number (DN_{12}) per pixel column. The ROIC ADC consists of a correlated double sampling (CDS) input stage with interleaved sample-and-hold paths and an auto-zero comparator with a single linear analog ramp. A high-speed serializer processes the output pixel data. The eCCD clock regime defines the detector system's integration time and determines the periodic restart of the ADC clocking regime. The phase-locked relation between the control signals of the ADC's CDS input stage (ϕ_r, ϕ_a, ϕ_{sh}, ϕ_{rd}) and the eCCD clock regime is crucial to guarantee the constant performance of the ADC, independent of the applied integration time (Fig. 2e).

For the eCCD charge domain, the flatband voltage shift of the input transfer gate $\Delta\phi_{dc}$ was extracted as the adjustment data for all other eCCD gates, ϕ_{1-4}, ϕ_{in}, ϕ_{tg}, and ϕ_{sw}, by assuming equal flatband voltage shifts for the eCCD gates and considering negligible TID-induced surface states, as well as buried channel eCCD operation without inversion during low state. The degradation of the ADC transfer function was quantified as an error function e(DN), enabling a mathematical correction via post-processing. Its coefficients had been fitted to the mean degradation of all four measured detectors. The SF gain loss ΔA_{sf} was revealed from the relative

changes in the SF circuit in the operation region. After performing the detector measurements, we extracted adjustment and correction data to evaluate which operation parameters were used to adapt the system.

To counteract potential changes in operational parameters due to aging or radiation, all crucial eCCD control nodes, such as transport gates, drain connections, reset gates, and the SF idle current source, were accessible via digital-to-analog converters (DACs) (Fig. 2d). Consequently, the CMOS-TDI detector system was flexible in responding to changes in the orbit environment and to different mission requirements during system design. The linear regression resulted in different flatband shift ratios for BSI and FSI vs. the radiation dose (Fig. 2c). The degradation of the ADC transfer curve revealed one degradation curve per radiation step and enabled a correction by the error function e(DN). Considering every measured radiation step, a marginal mean SF gain loss ratio was extracted (Fig. 2b). The changes could be contained by adjusting the SF idle current I_{sf} via a DAC (Fig. 2d).

The accuracy of the extraction method of the flatband voltage shift can be increased by utilizing physical simulation. The bidirectional design, including an even number of TDI gates, should be further analyzed to establish equal relations between the buried channel potentials and the depletion regions below the injection and readout sides and determine the resulting uncertainties for the two operating directions. The simulation shall consider the unique design properties of each overlapping poly-gate, including precise thickness and applied gate oxide voltage, which are major terms in the determination of the threshold voltage shift[33]. The applicability of e(DN) is limited to this specific ROIC design version. For every new design, the characterization should be verified, including validation of the function type of e(DN) to achieve the smallest residual error. In addition, we aim to incorporate radiation-hardening-by-design measures in the next revision of the ADC, such as implementation of enclosed layout transistors (ELT) and optimization of transistor aspect ratios to avoid parasitic leakage current[34–38]. Nevertheless, to improve accuracy, the present data set, based on four of 512 operating ROIC channels, could be expanded by measuring additional ROIC devices. The performance impact of the change in SF gain is secondary to the degradation in the ADC transfer function and the significant eCCD charge-domain misalignment.

Overall, adjustment data for the eCCD charge domain misalignment and the SF gain loss are available to perform a system adaptation of the CMOS-TDI detector. In addition, an error function can be used to post-process data sampled by the ROIC and to correct the ADC transfer function degradation.

Monitoring to verify the detector system performance

We equipped the CMOS-TDI detector system with in-orbit monitoring capability to unveil time-domain information of the eCCD output signal that was previously inaccessible during operation. Three inherent tests constituted an initialization phase that could be applied periodically to monitor the performance of the eCCD charge domain and the SF circuitry. The extraction of time-domain information of the eCCD output signal was realized by the subsampling operation mode. It combined equivalent time sampling (ETS) with CDS to derive time-domain information about the converter input signal (Fig. 3c)[39–44]. We used the impulse charge injection test to monitor the CTE (Fig. 3d), and the fill threshold test for the assessment of the flatband voltage shift[45].

Figure 3a shows the subsampling result for two eCCD outputs with different settling characteristics. It enabled a more accurate assessment of the signal settling characteristic and its relation to the ADC timing regime, without probing or adding load to any sensitive circuit node by design. Hence, it allowed for time-domain adjustment between the ADC regime and a degraded eCCD output signal by providing inherent detector feedback during operation in-orbit (Fig. 3b). For the impulse charge injection test, significant changes in the output impulse shape were observed during irradiation, with the output charge impulse changing drastically due to misalignment of the eCCD charge domain (Fig. 3e). The fill threshold test revealed a significant flatband voltage shift (Fig. 1b).

The subsampling test monitors any timing or level changes of the eCCD output signal. The subsampling output is proportional to the derivative of the ADC input signal or rather the output signal of the eCCD. Although time-domain information can be extracted from the results to detect relative changes during operation, they still include the asymmetric system response of the CDS input stage amplifier[40]. This should be considered in future research, investigating further absolute assessment of the original converter input signal or the eCCD output signal. The measurement results of the charge impulses confirm that the corresponding impulse charge injection test is highly suitable for monitoring changes in CTE, which are linked to MTF performance and enable in-orbit assessment of changes in image quality[31,32,46,47]. The established potential alignment of the eCCD buried-channel (transport), the corresponding input (injection), and output (readout) sections is significantly disturbed, which in turn affects the transfer conditions for the charge packets. Similar effects are reported, in which CTE degrades considerably due to charge-domain misalignment and the buildup of unwanted charge barriers[48]. The analysis using the EPER method clearly indicates the misalignment. To distinguish and characterize the different types of charge losses, future research should aim to enhance the in-orbit monitoring capabilities including first pixel edge response (FPER)[25]. The fill threshold test assesses the flatband voltage shift, which causes the reported CTE degradation (Fig. 1c). In addition, performing the test in orbit provides monitoring data about the real accumulated total ionizing dose.

Overall, performance monitoring is based on three inherent tests, including the extraction of previously inaccessible time-domain information from the eCCD output signal during operation via subsampling. It enables a more accurate assessment of the CMOS-TDI detector system's status in orbit and provides inherent detector feedback to conduct targeted dynamic adjustment of the detector system.

Dynamic degradation containment for constant image quality

To achieve a constantly high image quality and system performance over the lifetime in orbit, the extracted adjustment data was applied to the detector. We conducted an impulse charge injection test on one irradiated detector (110 krad(Si)) to assess the effect of detector system adaptation and demonstrate the containment of

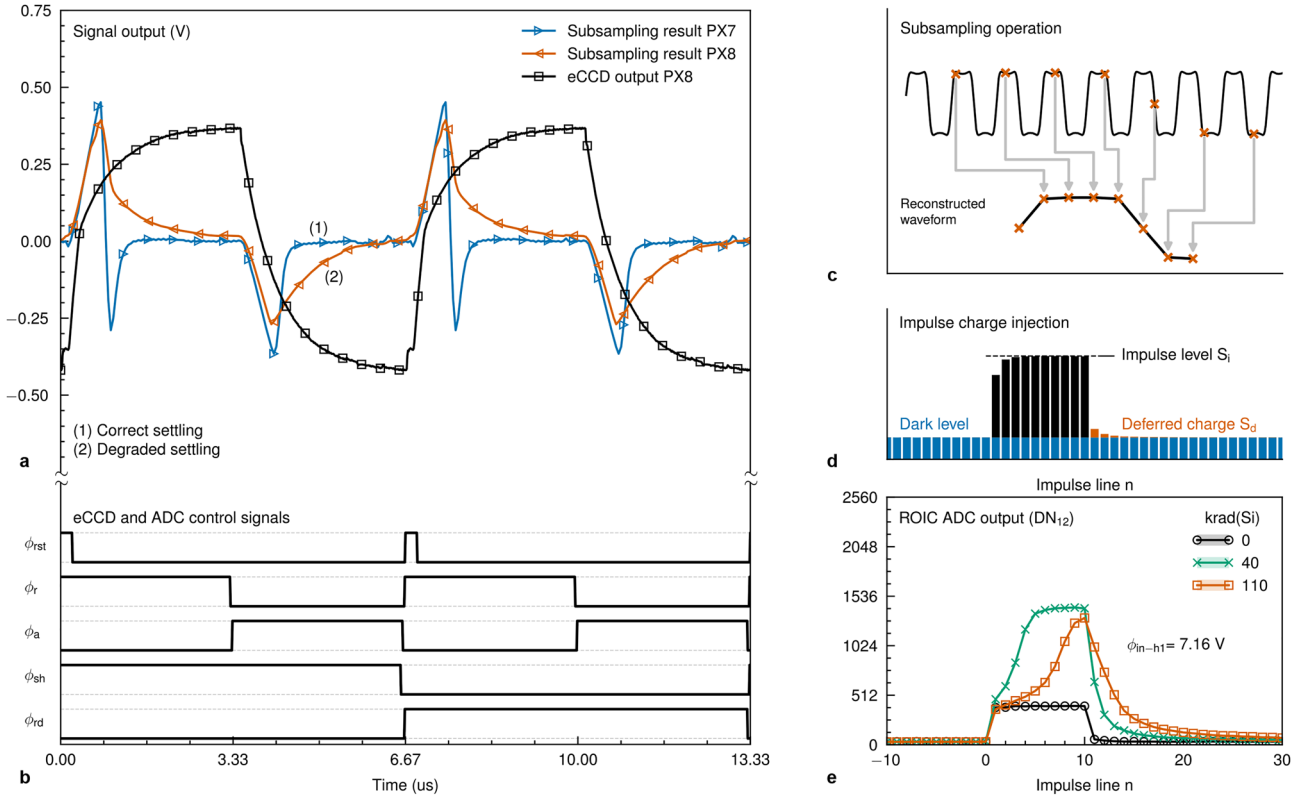


Fig. 3. The monitoring capability of the CMOS-TDI detector system. (**a**) Results of the subsampling operation mode: PX7 is directly connected from eCCD to ROIC and not accessible for external measurement, resulting in nominal bandwidth and settling time. In contrast, PX8 is externally loaded to access the circuit node via probing and, therefore, shows limited bandwidth (eCCD output PX8). The degraded settling (2) differs significantly from the correct settling (1), illustrating the monitoring of any timing or level changes during operation. (**b**) Schematic illustration of the eCCD and ADC control signals. All crucial eCCD and ADC control signals, such as ϕ_r, ϕ_a, ϕ_{sh}, and ϕ_{rd} can be reconciled with the time-domain monitoring result to maintain the inherent cross-domain signal constraints by reconfiguring the underlying detector state machine. (**c**) Schematic illustration of the subsampling operation mode as a form of signal reconstruction, adapted from[39]. (**d**) Impulse charge injection scheme for CTE calculation by the extended pixel edge response (EPER) method, indicating the key elements[25]. (**e**) Impulse charge injection result for different radiation doses, illustrating a drastic change in impulse shape above a radiation dose of 20 krad(Si) due to the misalignment of the eCCD charge domain.

TID-induced degradation. The eCCD charge domain and voltage domain were adjusted by $\Delta\phi_{dc}$ and ΔI_{sf}, respectively. In contrast, the ADC degradation was corrected mathematically using the inverse function of e(DN) to generate the adapted detector system. The SF gain loss was compensated by adjusting the idle current I_{sf} via a current source, which was controlled by a high-accuracy 14 bit DAC.

The flatband voltage shifts for the eCCD gates were compensated by reducing the gate potentials by the extracted voltage difference $\Delta\phi_{dc}$. Figure 4 illustrates the results of the impulse charge injection test before and after system adaptation. The absolute pre-radiation impulse level could not be recovered (Fig. 4a). The degraded charge train was compensated towards a more confined impulse with reduced charge losses, resembling the normalized original impulse shape (Fig. 4b). Hence, the adaptation improved the alignment of the eCCD charge domain setting, and the relative charge loss was reduced by a factor of 8.1 compared to the irradiated and misaligned system. The error function e(DN) enabled a non-compensatory mathematical correction for data sampled by the ROIC ADC, revealing the residual relative degradation after applying the correction on all four measured detectors below ±1% for the full dynamic range (Fig. 4c).

The charge injection level seems to be influenced by unequal flatband voltage shifts below the gates of the eCCD input section. The system adaptation may benefit from a more specific voltage shift extraction method based on physical simulation, and a higher relative accuracy of the DACs used for adjustment, especially at the very sensitive input section (ϕ_{id}, ϕ_{dc}, and ϕ_{in}). In summary, adapting the operation parameters during irradiation substantially improves geometric resolution in the flight direction by maintaining the CTE at the pre-radiation level. As the change in SF gain loss was minimal, the relative accuracy of the used DAC has to be reasonable, but in terms of upcoming highly integrated applications, relative accuracy may become a critical design issue. The compensation of the degradation in the ADC dynamic range is not possible, as there are

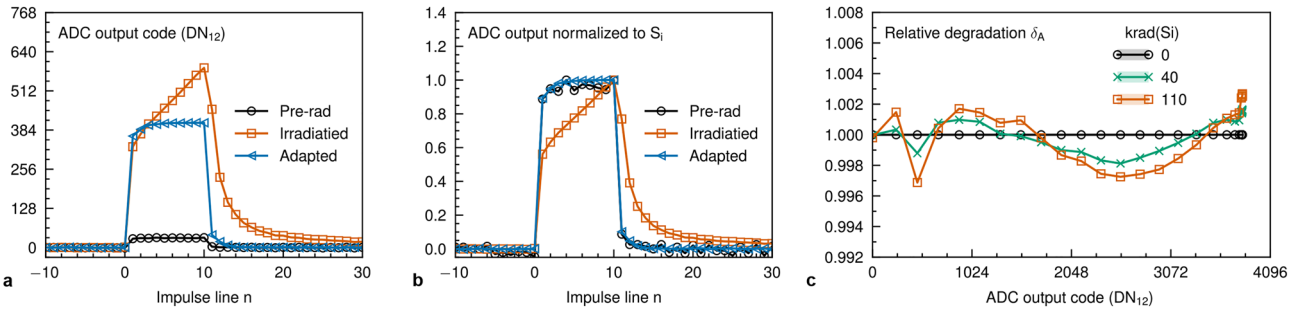


Fig. 4. Dynamic system adaptation for degradation containment. (**a**) Absolute result of the impulse charge injection test before (Irradiated, 110 krad(Si)) and after detector system adaptation (Adapted, 110 krad(Si)), compared with the pre-radiation result (Pre-rad), illustrating the reduction of the impulse level towards pre-radiation status. (**b**) Relative result of the impulse charge injection test before (Irradiated, 110 krad(Si)) and after detector system adaptation (Adapted, 110 krad(Si)), compared with the pre-radiation result (Pre-rad), showing the corrected charge train as an impulse with reduced charge loss and the resembled impulse shape of the pre-radiation status. (**c**) Residual relative ADC degradation after applying the inverse function of the error function e(DN) for different radiation doses on one exemplary detector, indicating a residual relative degradation of below ±0.5% for the full dynamic range.

currently no means of counteracting the effect of increased noise, namely, there are no adaptable operation parameters within the analog circuitry of the ADC input stage.

Overall, eCCD charge domain adjustments are crucial detector-oriented methods for the CMOS-TDI detector system to counteract TID-induced degradation. The investigation shows that dynamic adaptation of the detector system significantly contains the impact of radiation. The CTE after system adaptation accordingly reaches the pre-radiation level for pure buried-channel operation, which confirms that the contribution of bulk defects is negligible compared to with the TID-induced voltage barrier effects. The mathematical correction for the relative degradation in the ROIC ADC allows the TID-independent assessment of data recorded with the ADC.

Device compact modeling to predict radiation impact

Modeling the impact of radiation on the CMOS-TDI detector system enabled the prediction of TID-induced changes in the eCCD and ROIC. Initially, we elaborated extended device models using manufacturer and published experimental data for the eCCD voltage domain and ROIC ADC circuitry. We further adapted the initial models after validation by the system level results of the detector measurements. Within the validation, the results of the ADC transfer function test and the SF characterization were compared to the corresponding system simulation results based on the extended device model libraries (BSIM3)[49]. The identified relative degradations were used to adapt the underlying device models.

The function on mobility for ROIC and eCCD showed no influence on the performed comparison in the investigated dose range, hence, the resulting coefficients of the describing functions were set to zero. Additionally, the function type for the eCCD NMOS threshold voltage was changed from a quadradic polynomial to an empirical four-parameter saturating function, improving the model by decreasing the residual deviation between simulation and the results of the detector measurements. Figure 5a shows the achieved improvement for the ADC transfer function degradation. The matching between simulation and experimental data was significantly improved up to 10 krad(Si) and above 60 krad(Si), yielding an overall maximum deviation of 10% for the whole range of the input signal $\hat{u}$. The eCCD voltage domain degradation also showed improved model alignment with the experimental data (Fig. 5b).

The adapted models, following validation of the initial extended device models, provide more precise predictions of TID-induced effects on the ROIC and SF circuitry. However, the applied method for model adjustment is limited in accuracy due to the transfer of relative system-level measurement results to device models. Utilizing simplified test structures or single devices for the purpose of external validation may increase robustness and accuracy for both established model libraries[49,50]. The deviation in matching between 10 krad(Si) and 60 krad(Si) for the ROIC can be attributed to limitations of the simulation methodology used (SPICE). The effects of parasitic elements extracted from the layout cannot be considered due to the unavailability of layout data. The circuit consists of 186 transistors. Within the mentioned dose range, both parasitic elements and capacitive negative feedback have a significant impact on the convergence of the simulation. This results in higher complexity in the iterative simulation. Consequently, the achievable accuracy using a conventional SPICE approach should be interpreted as limited for the whole investigated dose range. In future research, performing parasitic extraction (PEX) and including the results in an enhanced simulation environment can improve the accuracy of the device models. In addition, migrating the device models to BSIM4, which incorporates more enhanced capacitive effects, can also increase confidence and resolve convergence problems in capacitive-sensitive parts of the circuit.

Overall, the extended device compact models adequately predict performance changes caused by TID in the ROIC and eCCD voltage domain for the examined detector system. They form the basis of a comprehensive

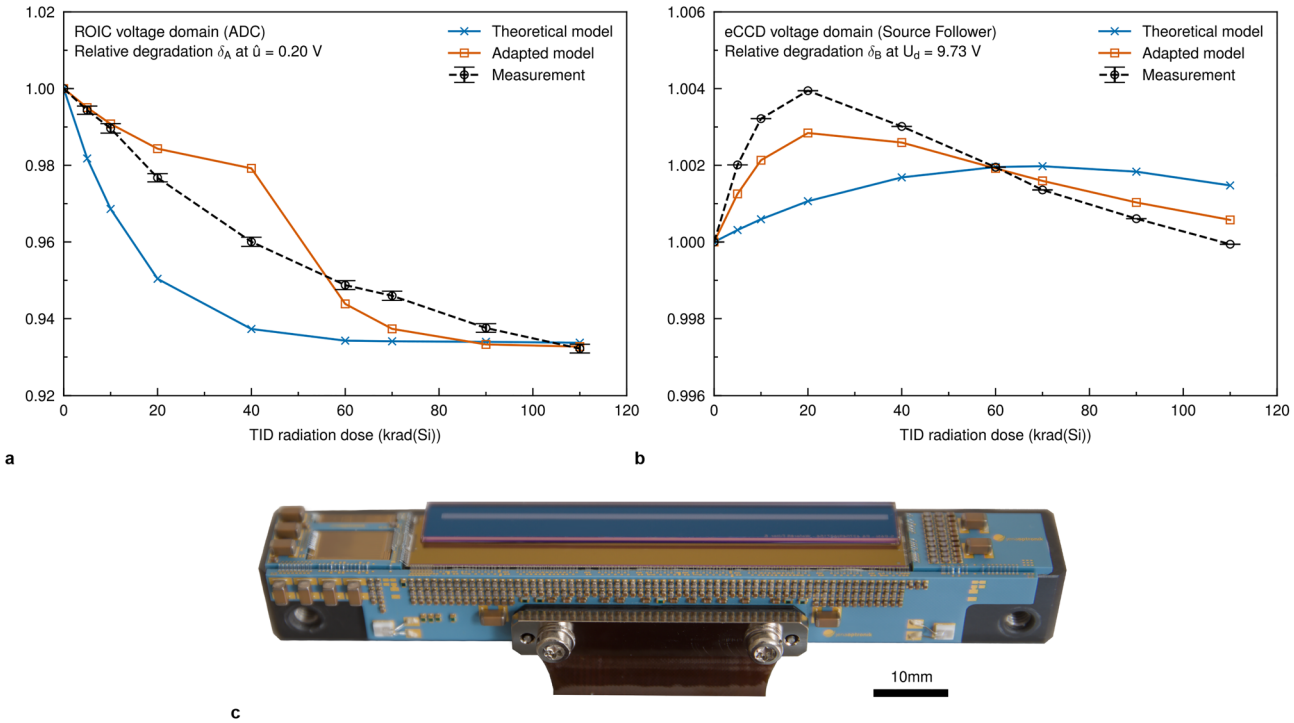


Fig. 5. Device compact modeling to predict radiation impact. (**a**) Model and measurement data of ROIC ADC degradation by increasing radiation dose for an input voltage of $\hat{u}$ = 0.2 V before and after model adaptation, indicating an improved overall matching between the adapted model and the measurement. (**b**) Model and measurement data of eCCD voltage domain (SF) degradation by increasing radiation dose for a gate voltage of U_d = 9.73 V before and after model adaptation, showing an improved overall matching between the adapted model and the measurement. (**c**) Highly-integrated detector model of the CMOS-TDI detector family, assembled on a ceramic carrier, including high-voltage drivers and optical filter. It constitutes a flexible detector module with 8092 7 × 7 µm pixels, capable of operating at a line rate of 75 kHz and using up to 128 TDI stages, Credit: German Aerospace Center (DLR), WR-HGE[9].

system model, including TID effects, to enable a more profound assessment of upcoming designs for the CMOS-TDI detector family (Fig. 5c). Future research should address the external validation on independent and simplified structures on the same CMOS technologies to enable the models to perform a reliable and independent performance prediction. The prediction can be further enhanced by including PEX into the established model flow to enable a comprehensive physical simulation of the eCCD and ROIC voltage domain.

Conclusion

In order to derive maximum benefit from the technological advance in sensor accuracy and sensitivity for space missions, it is crucial to contain the impact of the radiation environment on satellite imaging systems. The flexible architecture of the next-generation CMOS-TDI sensor system meets the very high optoelectronic requirements, while charge injection and subsampling ensure inherent monitoring of the detector performance and enable dynamic detector-targeted approaches to counteract TID-induced performance degradation during operation in orbit.

We found that system adaptation in the eCCD charge domain maintained performance at a consistently high level, and the compensation of the eCCD flatband voltage shift provided a significant reduction in the relative charge loss by a factor of 8.1, while the relative shape of the injected charge impulse could be completely restored. The CTE of the irradiated detector system was significantly increased and reached the pre-radiation level.

Overall, the investigation shows, that dynamic detector-oriented methods are able to efficiently contain systematic TID-induced degradation and may substantially contribute to achieve long-term reliability of CMOS-TDI sensor systems over lifetime in space missions. Performance changes caused by TID in both, ROIC and eCCD voltage domain, can be adequately predicted by compact device modeling for the examined detector system. It should be validated externally on simplified and independent CMOS structures and considered for general application in upcoming designs of the CMOS-TDI detector family. The reported extent of degradation containment, and thus the considerable gain in image quality, outweighs the effort for the implementation of additional control functionalities in CMOS-TDI sensor systems and may set a new standard for future missions.

Methods

All detector measurements were conducted unbiased, with all pins shorted together and grounded at a dose rate of 10 krad(Si)/h on four detectors. Pre-analysis revealed substantial bipolar effects in the eCCD. Additionally,

the current dose rate suggests a relatively low threshold for possible circuit failure[51]. Consequently, we decided to use an unbiased grounded radiation mode to minimize the risk of total device failure. Each test was performed iteratively, with intervals between ^{60}Co (γ) radiation exposure at steps 0, 5, 10, 20, 40, 60, 70, 90, and 110 krad(Si) by remote testing. The Gamma rays, which were emitted by ^{60}Co (γ) sources induce bulk defect induced dark current random telegraph signals (DC-RTS) through the generation of secondary electrons[29]. For the relatively highly doped buried channel in the examined detector system, DD effects were not noticeable and could be neglected inside the investigated radiation dose[30]. The detectors were measured at room temperature in the dark, with the light-sensitive area covered. The detector measurements included the following electrical tests:

ADC transfer function test The transfer function was determined by recording the ROIC ADC output code as a function of the differential input level $\hat{u}$ using a converter-synchronized external input signal to emulate an eCCD output signal[40].
Fill threshold test The input n+ drain voltage level, at which charge carriers start to reach the input gate ϕ_{in} through ϕ_{dc}, was quantified by iterating the low level of the input n$^+$ drain during constant charge injection (Fig. 2d)[39]. The DC-blocking gate ϕ_{dc} acted as a barrier to minority charge carriers injected via ϕ_{id}. If the applied voltage at ϕ_{dc} was more positive, a less positive low level of ϕ_{id} was sufficient to get the depletion region below ϕ_{in} filled with charge carriers. TID accumulated charge in all gate oxides of the eCCD. Consequently, the start of charge injection into the input gate ϕ_{in} occured earlier with increasing radiation dose D, resulting in a higher channel potential at the input n+ drain during fill-and-spill to initiate the fill operation. The difference in channel potential was directly assigned to the TID-induced shift of the input transfer gate ϕ_{dc} as a change in flatband voltage, given that the operating conditions avoid surface inversion (– 3.0 to 7.5 V). It was assumed that the flatband voltage shifts below all gates of the eCCD structure are identical.
Source follower characterization The eCCD SF circuitry transfer function was obtained by applying a DC voltage at the drain of the conducting reset transistor (Q1, Fig. 2d) and measuring the resulting DC voltage at the interface between the eCCD output and the ROIC ADC input with an external ADC[52].
Constant charge injection test Fill-and-Spill operation was conducted by maintaining a constant injection level at the input gate ϕ_{in}[39,53].
Impulse charge injection test The degradation of overall charge transport quality from injection to readout was obtained by injecting a charge impulse train with the applied input gate potential ϕ_{in-h1} and calculating the CTE by the extended pixel edge response (EPER) method[25,46]. The relative charge loss η was calculated by the relation between the deferred charge S_d and the last line of the impulse S_i (Fig. 3d):

$$\eta = \frac{S_d}{S_i} \tag{1}$$

Subsampling This operation mode was performed using the eCCD output signal generated by constant charge injection. Subsampling combined ETS with CDS to gain derived time-domain information of the converter input signal[39–43]. It was based on a specific configuration of the ROIC ADC, which originated from applying gated or boxcar integrators exclusively on periodic signals[44]. Constant charge injection provided a periodic signal at the eCCD output, emulating constant pixel values for each readout. The sampling window, which was much smaller than the period of the measured signal, was swept across it, producing at the output a lengthened replica of the input signal, i.e., a reconstructed waveform (Fig. 3c)[54]. The CDS architecture of the ADC input stage implied a crucial constraint for the acquired replica, namely that the subsampling output was proportional to the derivative of the converter input signal.

The tests of the ADC transfer function and the SF characterization were supported by a SPICE simulation bench that provided a representation of the experimental conditions to identify and attribute TID-induced errors in the voltage domain. In contrast, a corresponding physical simulation environment for the fill threshold test could not be established due to missing data. The evaluation focused on the relative degradation compared to the pre-radiation results, using the non-irradiated data as a calibration reference. The thermal activation energy Ea of the eCCD was determined by measuring the leakage current at various temperatures in a reverse-biased diode (7.0 V) formed by the p-substrate and the n-well (eCCD buried-channel).

Detector system adaption

The results of the detector measurements (ADC transfer function test, SF characterization, and fill threshold test) provided the data to correct the degradation effects on the ROIC voltage domain and to adjust operational parameters of the eCCD voltage domain and charge domain. The degradation of the ADC transfer function was extracted as an error function e(DN) by the following steps:

- A pre-radiation dark level correction of the ADC transfer function test was performed using this reference as the lowest value of the range of validity for e(DN).
- The error function (2) was fitted to the mean degradation results of all four measured detectors, with its coefficients α_1, β_1, α_2, and β_2 per measured radiation dose. The function type was selected for the lowest residual error across all four measured detectors.

$$e(DN) = \left((\alpha_1 - 1)e^{-\frac{DN}{\beta_1}} + 1\right)\left((\alpha_2 - 1)e^{-\frac{DN}{\beta_2}} + 1\right) \tag{2}$$

The inverse function of e(DN) was applied as a mathematical correction for this specific detector type, based on a known radiation dose D.

The eCCD voltage domain degradation was reflected in a loss of the SF gain A_{sf}. It was calculated by linear regression of the SF characterization results within the operating region (8.0 V < U_d < 11.0 V), yielding the TID-induced deviation ΔA_{sf} and the corresponding required change in SF idle current ΔI_{sf}.

The adjustment data for the eCCD charge domain (CCD gates) were extracted from the fill threshold test to assess the flatband voltage shift for the eCCD input transfer gate ($\Delta\phi_{dc}$). Data preprocessing was performed using the error function e(DN), eCCD voltage domain compensation, and dark level correction. The shift of ϕ_{dc} was directly assigned to the adjacent gate ϕ_{in}, the transport gates ϕ_1, ϕ_2, ϕ_3, and ϕ_4, and the output section (ϕ_{sw} and ϕ_{tg}), aiming to counteract degradation in the charge domain. The operation parameters of the detector system were updated by considering the extracted adjustment data of ΔI_{sf} and $\Delta\phi_{dc}$.

Finally, we conducted the impulse charge injection test on one of the four previously irradiated detectors to assess the effect of detector system adaptation and demonstrate the containment of TID-induced degradation. The mathematical correction using e(DN) was applied to the ROIC-sampled data.

Device compact modeling

Our approach to modeling TID-induced effects was based on a two-step degradation modeling process. Initially, we developed extended device models using manufacturer-provided and published experimental data. We additionally adapted the initial models after validation using the system level test results from the detector measurements.

In the first step, we theoretically derived the TID degradation for both implemented technologies, IHP-SG13S (ROIC) and IMS-L035-Opto (eCCD), using extended device models.

The IHP-SG13S TID radiation test report provided all the data necessary to directly determine the parametrization of the transistor models, specifically vth0 for the threshold voltage and u0 for the mobility[34,49]. The experimental radiation test data up to 500 krad(Si) showed a significant change in the transfer characteristic for exemplary high-voltage (HV) MOS transistors. The observed increase in drain current at zero gate voltage from 13 pA for a non-irradiated device to 21 µA at 200 krad(Si) and the threshold voltage shifts, stated up to -30 mV for PMOS and -200 mV for NMOS devices for a radiation dose of 200 krad(Si), have been assigned to radiation-dependent parameters u0 and vth0, respectively. Both parameters were implemented into an initial extended device model by a specific function of the dose D in krad(Si).

A more generic procedure was used for IMS-L035-Opto, based on published experimental data from a similar process, combined with the results of a formal guide on modeling the impact of radiation on CMOS structures, due to a lack of specific radiation test data for the investigated eCCD technology[23,55]. Therefore, the theoretical approach relied on detailed knowledge of the process design kit (PDK), including doping profiles, oxide thicknesses, and an initial pre-radiation device model for the implemented NMOS transistor. A polynomial function was used to extend the model parameters vth0 and u0 to fit the derived data.

We employed SPICE simulation, including extended device model libraries, to assess TID-induced degradation of the eCCD and ROIC voltage domain. It helped identify radiation-sensitive circuitry that could degrade performance and guided the selection of intermediate electrical tests during the detector measurements.

In the second step of the degradation modeling approach, the test results of the detector measurements at the system level were used to validate and, consequently, adapt the initial extended device models. In the course of model validation, the extended device models for the ROIC and the eCCD voltage domain were adapted, considering the deviations between the results of the detector measurements (ADC transfer function test and the SF characterization) and the SPICE simulation results by adjusting the parameters for threshold voltage and mobility as a function of the total ionizing dose parameter D.

Data availability

The datasets used and/or analyzed during the current study available from the corresponding author on reasonable request.

Received: 13 May 2026; Accepted: 15 September 2026
Published online: 24 September 2026

References

1. Sulaiman, N. N. et al. Radiation-induced degradation in optoelectronic devices for satellite applications: A review. *Discov. Mater.* **5**(1), 59. https://doi.org/10.1007/s43939-025-00185-y (2025).
2. Jerram, P. & Stefanov, K. CMOS and CCD image sensors for space applications. In *High Performance Silicon Imaging* 2nd edn (ed. Durini, D.) 255–287 (Woodhead Publishing, Cambridge, 2020).
3. Jiang, Y. et al. Research on proton displacement damage effects in charge-domain accumulation type TDI CMOS image sensors. *Radiat. Eff. Defects Solids* **179**(5–6), 811–822. https://doi.org/10.1080/10420150.2024.2311826 (2024).
4. Petersen, E. *Single Event Effects in Aerospace* (Wiley, Hoboken, 2011).
5. Fortescue, P. *Spacecraft Systems Engineering* 4th edn. (Wiley, West Sussex, 2011).
6. ECSS: ECSS-E-HB-10-12 Space Engineering—Calculation of Radiation and Its Effects and Margin Policy Handbook (accessed 2026-08-28). https://ecss.nl/wp-content/uploads/handbooks/ecss-e-hb/ECSS-E-HB-10-12A17December2010.pdf.
7. Twedt, K., et al. Calibration of NOAA-20 VIIRS reflective solar bands with combined solar diffuser and lunar data for NASA Collection 2 L1B. In: *Earth Observing Systems XXVII, vol. 12232, Art. no. 122320R* (SPIE, San Diego, 2022). https://doi.org/10.1117/12.2631700. International Society for Optics and Photonics.
8. Liu, Y.-K. et al. On-orbit radiometric calibration of the optical sensors on-board SuperView-1 satellite using three independent methods. *Opt. Express* **28**(8), 11085–11105. https://doi.org/10.1364/OE.388387 (2020).
9. Eckardt, A., et al. German CMOS-TDI technology for high-spatial and radiometric spaceborne application. In: *Earth Observing Systems XXX* Vol. 13611, Art. no. 1361104 (SPIE, San Diego, 2025). https://doi.org/10.1117/12.3063535.

10. Sanjeevi, S., et al. Teledyne's CMOS TDI detectors for remote sensing applications. In: *Earth Observing Systems XXX* vol. 13611, Art. no. 1361105 (SPIE, San Diego, 2025). https://doi.org/10.1117/12.3063924.
11. Mahato, S.B., et al. Multispectral CCD-in-CMOS Time Delay Integration Imager for High Resolution Earth Observation (2021). arXiv:2109.14532.
12. Ahmed, S., et al. Modelling charge transfer inefficiency in Gaia CCDs with in-flight and on-ground data. In: *X-Ray, Optical, and Infrared Detectors For Astronomy X* vol. 12191, Art. no. 121911G (SPIE, Montreal, 2022). https://doi.org/10.1117/12.2629273.
13. Hopkinson, G. R. Radiation effects on solid state imaging devices. *Radiat. Phys. Chem.* **43**(1), 79–91. https://doi.org/10.1016/0969-806X(94)90203-8 (1994).
14. Marcelot, O. et al. Radiation effects in CCD on CMOS devices: First analysis of TID and DDD effects. *IEEE Trans. Nucl. Sci.* **62**(6), 2965–2970. https://doi.org/10.1109/TNS.2015.2497405 (2015).
15. Wang, Z. et al. Evaluation of the degradation on a COTS linear CCD induced by total ionizing dose radiation damage. *J. Sens.* **201**(1), 9604042. https://doi.org/10.1155/2016/9604042 (2016).
16. Boychenko, D. et al. Total ionizing dose effects and radiation testing of complex multifunctional VLSI devices. *Facta Univ. Ser. Electron. Energ.* **28**(1), 153–164. https://doi.org/10.2298/FUEE1501153B (2015).
17. Layton, P., et al. TID performance degradation of high precision, 16-bit analog-to-digital converters. In: *2003 IEEE Radiation Effects Data Workshop* 6–10 (Monterey, 2003). https://doi.org/10.1109/REDW.2003.1281314.
18. Salih Alj, A. et al. Displacement damage effects on a CDTI-based CCD-on-CMOS: dark current and charge transfer inefficiency. *IEEE Trans. Nucl. Sci.* **72**(4), 1217–1227. https://doi.org/10.1109/TNS.2024.3480281 (2025).
19. Buggey, T. W. et al. Developing the active trap model for charge-coupled device charge transfer optimization in large-scale space missions. *J. Astron. Telesc. Instrum. Syst.* **8**(2), 028003. https://doi.org/10.1117/1.JATIS.8.2.028003 (2022).
20. Korea AeroSpace Administration (KASA): Press release 2026-03-17 (accessed 2026-03-23). https://www.kasa.go.kr/prog/plcyBrf/brief/kor/sub01_01_04/view.do.
21. Mueller, S., Weigel, R.& Koelpin, A. A survey on analog-to-digital converter performance with respect to ionizing radiation. In: *2017 17th European Conference on Radiation and Its Effects on Components And Systems (RADECS)* 536–539 (Geneva, 2017). https://doi.org/10.1109/RADECS.2017.8696150.
22. Hopkinson, G.R., Skipper, M.D. & Harboe-Sorensen, R. Radiation evaluation of low power CMOS 12-bit ADCs. In: *2000 IEEE Radiation Effects Data Workshop. Workshop Record. Held in Conjunction with IEEE Nuclear and Space Radiation Effects Conference (Cat. No.00TH8527)* 74–79 (Reno, 2000). https://doi.org/10.1109/REDW.2000.896273.
23. Osborn, J. V. et al. Total dose hardness of three commercial CMOS microelectronics foundries. *IEEE Trans. Nucl. Sci.* **45**(3), 1458–1463. https://doi.org/10.1109/23.685223 (1998).
24. Vici, A. et al. Performance and reliability degradation of CMOS image sensors in back-side illuminated configuration. *IEEE J. Electron Dev. Soc.* **8**, 765–772. https://doi.org/10.1109/JEDS.2020.2986729 (2020).
25. Janesick, J. R. *Scientific Charge-Coupled Devices* (SPIE Press, Bellingham, 2001).
26. İlik, S. & Yelten, M. B. Total ionizing dose (TID) impact on basic amplifier stages. *IEEE Trans. Device Mater. Reliab.* **23**(1), 51–57. https://doi.org/10.1109/TDMR.2022.3227766 (2023).
27. Barnaby, H. J. Total-ionizing-dose effects in modern CMOS technologies. *IEEE Trans. Nucl. Sci.* **53**(6), 3103–3121. https://doi.org/10.1109/TNS.2006.885952 (2006).
28. Adi, G. S., Kim, D.-S. & Kwon, I. Simulation-based analysis of total ionizing dose effects on low noise amplifier for wireless communications. *Nucl. Eng. Technol.* **56**(2), 568–574. https://doi.org/10.1016/j.net.2023.10.034 (2024).
29. Goiffon, V. et al. Gamma-ray induced displacement damage in silicon microvolumes: Single defect generation rate and random telegraph signal. *IEEE Trans. Nucl. Sci.* **73**(4), 1078–1088. https://doi.org/10.1109/TNS.2025.3648295 (2026).
30. Rax, B. G., Johnston, A. H. & Miyahira, T. Displacement damage in bipolar linear integrated circuits. *IEEE Trans. Nucl. Sci.* **46**(6), 1660–1665. https://doi.org/10.1109/23.819135 (1999).
31. Piechaczek, D. S. et al. Analytical model of free charge transfer in charge-coupled devices. *Solid-State Electron.* **199**, 108513. https://doi.org/10.1016/j.sse.2022.108513 (2023).
32. Liu, J. et al. Total ionizing dose and annealing effects in TDI CMOS image sensors. *IEEE Sens. J.* **25**(23), 42675–42682. https://doi.org/10.1109/JSEN.2025.3622927 (2025).
33. Dressendorfer, P. V. Radiation effects on MOS devices and circuits. In *Ionizing Radiation Effects in MOS Devices and Circuits* (eds Ma, T. P. & Dressendorfer, P. V.) 256–332 (Wiley, New York, 1989).
34. Schmidt, J. Leibniz-Institut für innovative Mikroelektronik (IHP) (2021) (TID) Test Report Rev. 1.0. Test Report unpublished IHP SG13RH Total Ionizing Dose.
35. Huang, W. et al. Design of 30 V high-voltage low-power radiation-tolerant analog switch IC. *IEEE Trans. Nucl. Sci.* **69**(4), 883–889. https://doi.org/10.1109/TNS.2022.3151409 (2022).
36. Vaz, P. I. Improving TID radiation robustness of a CMOS OxRAM-based neuron circuit by using enclosed layout transistors. *IEEE Trans. Very Large Scale Integr. VLSI Syst.* **29**(6), 1122–1131. https://doi.org/10.1109/TVLSI.2021.3067446 (2021).
37. İlık, S., et al. Comparison of ELTs with different shapes and a regular layout transistor in 180 nm CMOS process. In: *2019 16th International Conference on Synthesis, Modeling, Analysis and Simulation Methods and Applications to Circuit Design (SMACD)* 21–24 (Lausanne, 2019). https://doi.org/10.1109/SMACD.2019.8795230.
38. Snoeys, W. et al. Layout techniques to enhance the radiation tolerance of standard CMOS technologies demonstrated on a pixel detector readout chip. *Nucl. Instrum. Methods Phys. Res. Sect. A* **439**(2), 349–360. https://doi.org/10.1016/S0168-9002(99)00899-2 (2000).
39. Buschek, J., et al. In-orbit real-time CMOS TDI detector validation and control to meet constant imaging quality over the mission life time. In: *Earth Observing Systems XXVII* vol. 12232, Art. no. 1223205 (SPIE, San Diego, 2022). https://doi.org/10.1117/12.2631978. International Society for Optics and Photonics.
40. Buschek, J., et al. In-orbit VNIR sensor quality validation. In: *Sensors, Systems, and Next-Generation Satellites XXVII* vol. 12729, Art. no. 1272913 (SPIE, Amsterdam, 2023). https://doi.org/10.1117/12.2680166. International Society for Optics and Photonics.
41. Pitcher, A. D. et al. Accurate high-speed equivalent-time sampling receiver: Architecture and performance metrics. *IEEE Trans. Instrum. Meas.* **74**, 8006015. https://doi.org/10.1109/TIM.2025.3604952 (2025).
42. Sasaki, Y., et al. Highly efficient waveform acquisition condition in equivalent-time sampling system. In: *2018 IEEE 27th Asian Test Symposium (ATS)* 197–202 (Hefei, 2018). https://doi.org/10.1109/ATS.2018.00045.
43. Slovak, S., et al. Wideband receiver for UWB radars. In *2019 29th International Conference Radioelektronika* 128–131 (Pardubice, Czech Republic, 2019). https://doi.org/10.1109/RADIOELEK.2019.8733573.
44. Institute of Electrical and Electronics Engineers, Inc. (IEEE): *Std 1057-2017, Standard for Digitizing Waveform Recorders* (IEEE, New York, 2018).
45. Crowley, C. et al. Gaia data release 1—on-orbit performance of the Gaia CCDs at L2. *Astron. Astrophys.* **595**, 6. https://doi.org/10.1051/0004-6361/201628990 (2016).
46. De Moor, P., et al. Enhanced time delay integration imaging using embedded CCD in CMOS technology. In: *2014 IEEE International Electron Devices Meeting* 4.6.1–4.6.4 (San Francisco, 2014). https://doi.org/10.1109/IEDM.2014.7046984.
47. Marcelot, O. et al. Study of CCD transport on CMOS imaging technology: Comparison between SCCD and BCCD, and ramp effect on the CTI. *IEEE Trans. Electron. Dev.* **61**(3), 844–849. https://doi.org/10.1109/TED.2014.2298693 (2014).
48. Salih Alj, A. et al. Total ionizing dose effects on a CDTI-based CCD-on-CMOS through buildup of interface traps and oxide charges. *IEEE Trans. Nucl. Sci.* **71**(8), 1774–1782. https://doi.org/10.1109/TNS.2024.3358381 (2024).

49. İlik, S. et al. Modeling of total ionizing dose degradation on 180-nm n-MOSFETs using BSIM3. *IEEE Trans. Electron. Dev.* **66**(11), 4617–4622. https://doi.org/10.1109/TED.2019.2926931 (2019).
50. Petrosyants, K.O., Kharitonov, I.A. & Sambursky, L.M. SOI/SOS MOSFET universal compact SPICE model with account for radiation effects. In: *EUROSOI-ULIS 2015: 2015 Joint International EUROSOI Workshop and International Conference on Ultimate Integration on Silicon* 304–308 (Bologna, 2015). https://doi.org/10.1109/ULIS.2015.7063834.
51. Fleetwood, D. M. Radiation effects in a post-Moore world. *IEEE Trans. Nucl. Sci.* **68**(5), 509–545. https://doi.org/10.1109/TNS.2021.3053424 (2021).
52. Gao, C. et al. A novel source-drain follower for monolithic active pixel sensors. *Nucl. Instrum. Methods Phys. Res. Sect. A* **831**, 147–155. https://doi.org/10.1016/j.nima.2016.03.074 (2016).
53. Theuwissen, A.J.P. Solid-state imaging with charge-coupled devices. In: *Solid-State Science and Technology Library* vol. 1 (Kluwer Academic Publishers, Dordrecht, 1995).
54. Yamamoto, S., et al. Metallic ratio equivalent-time sampling: A highly efficient waveform acquisition method. In *2021 IEEE 27th International Symposium on On-Line Testing and Robust System Design (IOLTS)* 1–6 (2021). https://doi.org/10.1109/IOLTS52814.2021.9486692.
55. Cadence: Application Note: Radiation Effect Modeling. pspice.com/resources/application-notes/radiation-effect-modeling (Accessed 06-01-2026) (2016).

Acknowledgements

We would like to thank the entire development team of the CMOS-TDI sensor, composed of representatives of DLR-WR (German Aerospace Center, Institute of Space Research), EURECA, IHP (Leibniz Institute for High Performance Microelectronics), IMS (Fraunhofer Institute for Microelectronic Circuits and Systems), and JOP (Jena Optronik). We would also like to thank KARI (Korea Aerospace Research Institute) for their support, and Alina Dittwald for supervising the radiation tests at HZB (Helmholtz-Zentrum Berlin).

Author contributions

J. Buschek: Concept, methods, visualization, text draft, text finalization, project administration, testing, validation, simulation, software; E. Chernyavskiy: methods, testing, modelling, validation; G. Kahmen: Concept; A. Eckardt: Concept.

Funding

Open Access funding enabled and organized by Projekt DEAL. This research did not receive funding.

Declarations

Competing interests

The authors declare no competing interests.

Additional information

Supplementary Information The online version contains supplementary material available at https://doi.org/10.1038/s41598-026-72300-9.

Correspondence and requests for materials should be addressed to J.B.

Reprints and permissions information is available at www.nature.com/reprints.

Publisher's note Springer Nature remains neutral with regard to jurisdictional claims in published maps and institutional affiliations.

Open Access This article is licensed under a Creative Commons Attribution 4.0 International License, which permits use, sharing, adaptation, distribution and reproduction in any medium or format, as long as you give appropriate credit to the original author(s) and the source, provide a link to the Creative Commons licence, and indicate if changes were made. The images or other third party material in this article are included in the article's Creative Commons licence, unless indicated otherwise in a credit line to the material. If material is not included in the article's Creative Commons licence and your intended use is not permitted by statutory regulation or exceeds the permitted use, you will need to obtain permission directly from the copyright holder. To view a copy of this licence, visit http://creativecommons.org/licenses/by/4.0/.

© The Author(s) 2026